

Topological spin excitations in non-Hermitian spin chains with a generalized kernel polynomial algorithm

Guangze Chen,¹ Fei Song,^{2,*} and Jose L. Lado^{1,†}

¹*Department of Applied Physics, Aalto University, 02150 Espoo, Finland*
²*Institute for Advanced Study, Tsinghua University, Beijing, 100084, China*

(Dated: March 10, 2023)

Spectral functions of non-Hermitian Hamiltonians can reveal the existence of topologically non-trivial line gaps and the associated topological edge modes. However, the computation of spectral functions in a non-Hermitian many-body system remains an open challenge. Here, we put forward a numerical approach to compute spectral functions of a non-Hermitian many-body Hamiltonian based on the kernel polynomial method and the matrix-product state formalism. We show that the local spectral functions computed with our algorithm reveal topological spin excitations in a non-Hermitian spin model, faithfully reflecting the non-trivial line gap topology in a many-body model. We further show that the algorithm works in the presence of the non-Hermitian skin effect. Our method offers an efficient way to compute local spectral functions in non-Hermitian many-body systems with tensor-networks, allowing to characterize line gap topology in non-Hermitian quantum many-body models.

Non-Hermitian (NH) Hamiltonians have risen as a rich framework to describe the post-selected quantum dynamics of open quantum systems[1–3]. NH Hamiltonians have been found to host a variety of phenomena lacking a counterpart in Hermitian systems, including the non-Hermitian skin effect (NHSE)[4–12]. In addition, NH Hamiltonians exhibit unique topological properties: a topologically non-trivial gap can either be a line gap or a point gap[13–15]. The line gap is a generalization of the spectral gap in Hermitian systems, and a topologically non-trivial line gap is associated with topological edge modes in open boundary conditions[14]. The point gap topology is unique for non-Hermitian systems and it encodes the origin of NHSE[16–18]. Recently, the generalization of NH topology as well as other interesting aspects of NH physics such as parity-time symmetry breaking[19–21] and exceptional points[22–25] to NH many-body systems have attracted much interest[26–30].

Despite the intense interest in the study of NH many-body physics, efficient numerical tools are lacking. In the case of interacting one-dimensional problems, conventional tools to study Hermitian many-body systems based on density matrix renormalization group (DMRG)[31] cannot be directly applied to study NH many-body systems. In Hermitian many-body systems, local spectral functions can be computed efficiently for large-size systems within the DMRG framework using correction vector methods[32, 33], time-evolution[34, 35] or kernel polynomial algorithms[36–38]. However, for NH many-body Hamiltonians, the kernel polynomial method (KPM) does not apply directly[39], and an efficient algorithm to compute local spectral functions in NH many-body systems is lacking. The computation of local spectral functions of many-body excitations allow revealing many-body topological modes[38], and therefore would be of key interest to address topological interacting NH many-body models, in particular with a nontrivial line

gap.

Here, we put forward a many-body non-Hermitian kernel polynomial method (NHKPM)[40] to compute local spectral functions in NH many-body systems. We implement a KPM-based algorithm to compute the local spectral functions, where matrix-product states (MPS) are used to represent the states. We show that this method reveals topological many-body spin excitations in a NH spin chain with non-trivial line gap topology. We further show that this method provides faithful results in the presence of NHSE. Our results put forward a many-body algorithm to efficiently compute spectral functions in NH many-body systems, which in particular allows to characterize line gap topology in NH many-body systems.

We first summarize how KPM is used to compute local spectral functions in Hermitian spin systems. For a Hermitian $S = 1/2$ Hamiltonian H_0 , the local spectral density of $S_z = \pm 1$ excitations is given by the local spin structure factor:

$$\begin{aligned} \rho(E, l) = & \langle \text{GS} | S_l^- \delta(E + E_{\text{GS}} - H_0) S_l^+ | \text{GS} \rangle \\ & + \langle \text{GS} | S_l^+ \delta(E + E_{\text{GS}} - H_0) S_l^- | \text{GS} \rangle \end{aligned} \quad (1)$$

where $|\text{GS}\rangle$ and E_{GS} are the ground state and its energy, and $S_l^\pm = S_l^x \pm iS_l^y$ where l is the site index. Such local spin structure factor reveals topological spin excitations[38], which can be probed with scanning tunneling microscopy [41–45]. Since the eigenvalues of H_0 are bounded, we can perform a shifting and a rescaling on H_0 such that $E_{\text{GS}} = 0$ and the eigenvalues lie in $[0, 1)$. In such case, $\rho(E \in [0, 1), l)$ is a bounded single-variable function for fixed l , which is a crucial property that allows it to be expanded in Chebyshev polynomials $T_n(E) = \cos(n \arccos E)$:

$$\rho(E, l) = \frac{1}{\pi\sqrt{1-E^2}} \left(\mu_0 + 2 \sum_{n=1}^{\infty} \mu_n T_n(E) \right) \quad (2)$$

where the coefficients satisfy $\mu_n = \int_{-1}^1 dE \rho(E, l) T_n(E) = \langle \text{GS} | S_l^- T_n(H_0) S_l^+ | \text{GS} \rangle + \langle \text{GS} | S_l^+ T_n(H_0) S_l^- | \text{GS} \rangle$. Using the recursion relation of Chebyshev polynomials: $T_{n+1}(x) = 2xT_n(x) - T_{n-1}(x)$, the first term of μ_n can be computed as $\mu_n = \langle v | v_n \rangle$ where $|v\rangle = S_l^+ | \text{GS} \rangle$ and

$$\begin{aligned} |v_{n+1}\rangle &= 2H_0|v_n\rangle - |v_{n-1}\rangle \\ |v_0\rangle &= |v\rangle, |v_1\rangle = H_0|v\rangle, \end{aligned} \quad (3)$$

and similarly for the second term. The recursive structure of Eq. (3) allows the efficient computation of μ_n and $\rho(E, l)$. Furthermore, its simple algebraic structure allows it to be implemented with MPS representation of states, where the ground state can be computed with DMRG. Finally, Eq. (2) is approximated with a truncation of the summation to N^{th} order, where a Jackson kernel $g_n^N = \frac{(N-n+1) \cos \frac{n\pi}{N+1} + \sin \frac{n\pi}{N+1} \cot \frac{\pi}{N+1}}{N+1}$ is multiplied to the coefficients μ_n to damp Gibbs oscillations[36].

We now generalize Eq. (1) to an open spin system described with an effective NH spin Hamiltonian H . Unlike a Hermitian Hamiltonian, a NH Hamiltonian generally has a complex spectrum $\{E_n \in \mathbb{C}\}$. In addition, the left eigenvector $|\Psi_{L,n}\rangle$ and the right eigenvector $|\Psi_{R,n}\rangle$ corresponding to the same eigenvalue E_n of H are generally different and satisfy $\langle \Psi_{L,m} | \Psi_{R,n} \rangle = \delta_{mn}$. The eigen-decomposition of H is: $H = \sum_n E_n |\Psi_{R,n}\rangle \langle \Psi_{L,n}|$. Thus, we define the local dynamical spin correlator as:

$$\begin{aligned} \mathcal{S}(\omega, l) &= \langle \text{GS}_L | S_l^- \delta^2(\omega + E_{\text{GS}} - H) S_l^+ | \text{GS}_R \rangle \\ &+ \langle \text{GS}_L | S_l^+ \delta^2(\omega + E_{\text{GS}} - H) S_l^- | \text{GS}_R \rangle, \end{aligned} \quad (4)$$

where ω is a complex number, $|\text{GS}_{L,R}\rangle$ are left and right eigenvectors corresponding to the eigenvalue of smallest real part[29, 46], and $\delta^2(\omega - H) = \sum_n \delta(\Re(\omega - E_n)) \delta(\Im(\omega - E_n)) |\Psi_{R,n}\rangle \langle \Psi_{L,n}|$. Since ω is complex, $\mathcal{S}(\omega, l)$ is no longer a function of a single variable, and does not have the Chebyshev expansion Eq. (2) that allows it to be computed with KPM[47].

We now present how an NHKPM algorithm[48] allows to efficiently compute Eq. (4), and more generally, generic spectral functions of the form:

$$f(\omega) = \langle \psi_L | \delta^2(\omega - H) | \psi_R \rangle \quad (5)$$

where $|\psi_L\rangle, |\psi_R\rangle$ are arbitrary states. The key observation is, although Eq. (5) cannot be computed with KPM directly, it can be related to the spectral functions of the Hermitized form of $\omega - H$:

$$\mathcal{H} = \begin{pmatrix} & \omega - H \\ \omega^* - H^\dagger & \end{pmatrix}. \quad (6)$$

In particular, using $\partial_{\omega^*}(1/\omega) = \pi \delta(\Re(\omega)) \delta(\Im(\omega))$ [49], we can rewrite Eq. (5) as

$$f(\omega) = \frac{1}{\pi} \partial_{\omega^*} G(E=0) \quad (7)$$

where $G(E) = \langle \text{L} | (E - \mathcal{H})^{-1} | \text{R} \rangle$ is the Green's function of \mathcal{H} with $|\text{L}\rangle = \begin{pmatrix} 0 \\ |\psi_L\rangle \end{pmatrix}$ and $|\text{R}\rangle = \begin{pmatrix} |\psi_R\rangle \\ 0 \end{pmatrix}$. Since \mathcal{H} is

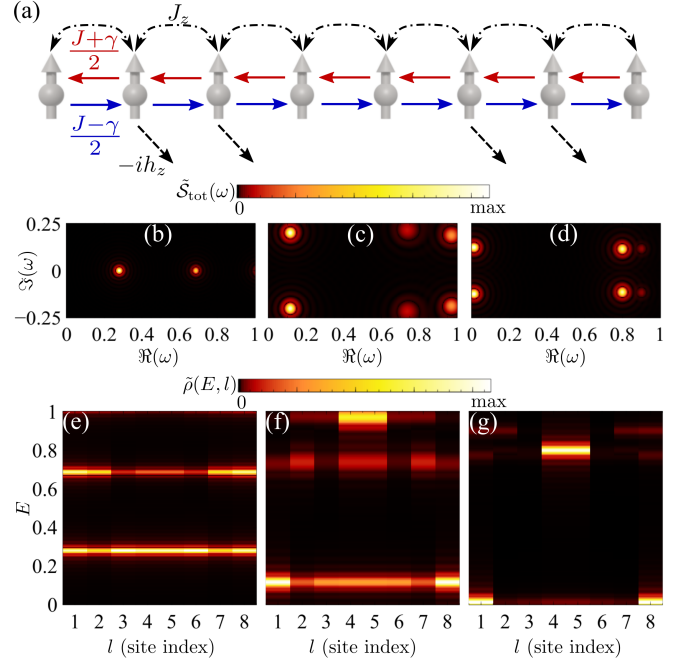


FIG. 1. (a) Sketch of the model Hamiltonian H in Eq. (9). (b-d) Total dynamical spin correlator $\tilde{\mathcal{S}}_{\text{tot}}(\omega)$ of H with $L = 8$, $\gamma = 0$ and (b) $h_z = 0$, (c) $h_z = J$, (d) $h_z = 2J$. (e-g) Projected local dynamical structure factor $\tilde{\rho}(E, l)$ corresponding to cases (b-d), respectively. Topological spin excitations with almost zero real energy are revealed in (g).

Hermitian, its Green's function $G(E)$ has the Chebyshev expansion Eq. (2), resulting in an expansion of $f(\omega)$ in Chebyshev polynomials of \mathcal{H} :

$$f(\omega) = \frac{2}{\pi^2} \sum_{n=1}^{\infty} (-1)^{n+1} \langle \text{L} | \partial_{\omega^*} T_{2n-1}(\mathcal{H}) | \text{R} \rangle \quad (8)$$

with the recursion relation $\partial_{\omega^*} T_{n+1}(\mathcal{H}) = 2 \begin{pmatrix} 0 & 0 \\ 1 & 0 \end{pmatrix} T_n(\mathcal{H}) + 2\mathcal{H} \partial_{\omega^*} T_n(\mathcal{H}) - \partial_{\omega^*} T_{n-1}(\mathcal{H})$. Finally, the above recursion relation on $T_n(\mathcal{H})$ is transformed into an update of vectors, similar to Eq. (3), allowing $f(\omega)$ to be computed with KPM. We use an MPS representation for the states $S_l^\pm | \text{GS}_{L,R} \rangle$ in the computation of Eq. (4), which enables computation for large size systems. We use a Krylov-Schur algorithm[50] to compute the states with the smallest real part[51].

We now use the NHKPM to identify the topological end modes emerging in a NH many-body system. We take the following NH $S = 1/2$ chain with antiferromagnetic exchange $J = 1$ (Fig.1(a)):

$$\begin{aligned} H &= \sum_{l=1}^{L-1} \left(\frac{J+\gamma}{2} S_l^+ S_{l+1}^- + \frac{J-\gamma}{2} S_l^- S_{l+1}^+ + J_z S_l^z S_{l+1}^z \right) \\ &+ \sum_{l=1}^L i h_l^z S_l^z \end{aligned} \quad (9)$$

where $h_l^z = -h_z$ if $l \bmod 4 = 2, 3$ and $h_l^z = 0$ otherwise. It is first illustrative to perform a Jordan-Wigner transformation to Eq. (9), leading to a NH interacting spinless fermion model:

$$\begin{aligned} \tilde{H} = & \sum_{l=1}^{L-1} \left(\frac{J+\gamma}{2} c_l^\dagger c_{l+1} + \frac{J-\gamma}{2} c_{l+1}^\dagger c_l \right. \\ & \left. + J_z (c_l^\dagger c_l - \frac{1}{2})(c_{l+1}^\dagger c_{l+1} - \frac{1}{2}) \right) + \sum_{l=1}^L i h_l^z (c_l^\dagger c_l - \frac{1}{2}). \end{aligned} \quad (10)$$

When $J_z = 0$, Eq. (10) becomes a non-interacting spinless fermion model, which for $\gamma = 0$ and non-zero h_z is known to give rise to topological end states whose real part of the energy is 0[52]. The bulk topology of this model is characterized by a hidden Chern number which faithfully predicts the number of stable end states with purely imaginary energy[52, 53]. It has been shown that in the presence of a finite interaction J_z , a sufficiently large h_z would still give rise to the topological end states[54]. In the following we explore the non-Hermitian many-body topology of the model via computing dynamical excitations using the NHKPM algorithm, both in the absence and presence of NHSE. For concreteness we take $J_z = 1/2J$, yet analogous results can be obtained for general values of J_z .

We first focus on a chain of length $L = 8$ in which we can implement the NHKPM method exactly with exact diagonalization as a benchmark. We first compute the total dynamical spin correlator, defined as:

$$\tilde{S}_{\text{tot}}(\omega) = \left| \sum_{l=1}^L \mathcal{S}(\omega, l) \right| \quad (11)$$

where $\mathcal{S}(\omega, l)$ is defined in Eq. (4) [55]. The total dynamical spin correlator reveals the energy of the states that have finite overlap with the ground state with one $S_z = \pm 1$ excitation. We see that as h_z increases, the real part of the energy of the lowest excited states is shifted towards 0, whereas the higher states are shifted away from 0 (Figs.1(b-d)). To see if the lowest excited states are topological end states, we compute the projected local dynamical structure factor, defined as

$$\tilde{\rho}(E \in \mathbb{R}, l) = \left| \int \mathcal{S}(E + iy, l) dy \right|. \quad (12)$$

This quantity identifies the local spectral density of $S_z = \pm 1$ excitations at a given real energy E . In particular, when H is Hermitian, $\tilde{\rho}(E, l)$ is reduced to the local spin structure factor defined in Eq. (1). Figs.1(e-g) shows $\tilde{\rho}(E, l)$ for different values of h_z , we see that for $h_z = 0$ the lowest states show non-vanishing spectral density in the bulk. As h_z increases to $h_z = J$ the spectral density in the bulk reduces, and eventually for sufficiently large $h_z = 2J$ the states become localized at the ends, reflecting the non-trivial line topology in the bulk. Due to

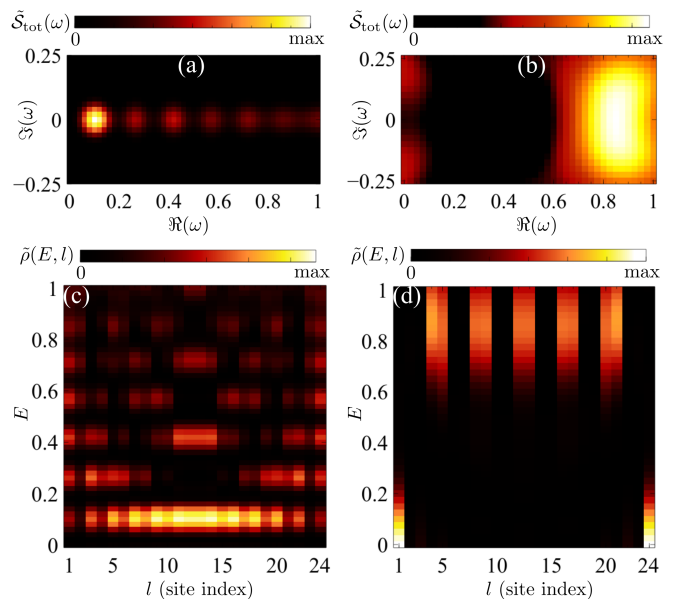


FIG. 2. (a,b) Total dynamical spin correlator $\tilde{S}_{\text{tot}}(\omega)$ of H defined in Eq. (9) with $L = 24$, $\gamma = 0$ and (a) $h_z = 0$ and (b) $h_z = J$. $\tilde{S}_{\text{tot}}(\omega)$ reveals a many-body line gap in (b). (c,d) Projected local dynamical structure factor $\tilde{\rho}(E, l)$ corresponding to cases (a,b), respectively. $\tilde{\rho}(E, l)$ reveals topological many-body excitations in (d), indicating that the line gap in (b) is topological.

the short chain length, finite-size effects prevent clearly observing topological end states for $h_z = J$ due to hybridization.

To approach the thermodynamic limit and demonstrate the capabilities of the NHKPM algorithm, we now move on to consider a chain of length $L = 24$. As these systems are too large to be treated by exact diagonalization, we now use a full tensor-network implementation with MPS in the NHKPM algorithm. The total dynamical spin correlator $\tilde{S}_{\text{tot}}(\omega)$ and the projected local dynamical structure factor $\tilde{\rho}(E, l)$ are computed for $h_z = 0$ and $h_z = J$ in this case (Fig.2). We see from Figs.2(a,b) that for $h_z = J$ there are clearly 2 states close to 0 real energy, and are isolated from the higher states with a line gap, whereas for $h_z = 0$ there is no such behavior. From Figs.2(c,d) we can observe the topological end states for $h_z = J$, whereas for $h_z = 0$ the lowest states are mainly distributed in the bulk. These show that the model Eq. (9) is not topological for $h_z = 0$, and is topological for $h_z = J$ even in the presence of many-body interactions.

We now consider a finite γ term, which is known to give rise to the NHSE[4–6]. In the non-interacting limit, the spectrum of H in the presence of NHSE is known to be drastically different under different boundary conditions: in the thermodynamic limit, the spectrum of H is purely real under open boundary condition (OBC), and features a point gap under periodic boundary condition (PBC). On the contrary, the spectrum of the Hermitized

Hamiltonian \mathcal{H} is not sensitive to boundary conditions: in the thermodynamic limit, the spectrum is the same under both boundary conditions except that when ω lies in the point gap of H , the spectrum under OBC shows more topological zero modes than that under PBC[16, 56]. It is due to the contribution of these additional zero modes to the Green's function of \mathcal{H} in Eq. (7) that allows faithfully computing the spectral function of H using NHKPM[57], despite the different sensitivities of the spectral functions of H and \mathcal{H} to the boundary condition. In the interacting case, the spectrum of H has no point gaps in the thermodynamic limit, and the above analysis no longer holds. Thus, it is unclear whether the algorithm allows for comparable accuracy, which we examine below. It is worth noting that the case $\gamma < J$ reduces to $\gamma = 0$ under a similarity transformation to H :

$$T = e^{\sum_l l \alpha S_l^z}, \alpha = \ln r, r = \sqrt{\frac{J + \gamma}{J - \gamma}} \quad (13)$$

$$TH(J, \gamma, J_z, h_z)T^{-1} = H'(J', 0, J_z, h_z).$$

The new uniform exchange is $J' = \sqrt{(J + \gamma)(J - \gamma)}$ which is approximately J for $\gamma = 0.1J$. This similarity transformation changes the spectral function Eq. (4) for H to the same spectral function for H' , leading to dynamical correlators analogous to the $\gamma = 0$ case for $\gamma \ll J$. As a benchmark, we compute both $\tilde{S}_{\text{tot}}(\omega)$ and $\tilde{\rho}(E, l)$ for H with $L = 8$, $h_z = 2J$ and $\gamma = 0.1J$ under OBC (Figs.3(a) and (c)), where the results are analogous to Figs.1(d) and (g), demonstrating that the NHKPM faithfully computes both spectral functions. We also show $\tilde{S}_{\text{tot}}(\omega)$ for H under the same set of parameters under PBC, where faithful results are obtained: the two end states with almost 0 real energy under OBC vanish under PBC. We also compute $\tilde{\rho}(E, l)$ for a longer chain with $L = 24$, $h_z = J$ and $\gamma = 0.1J$ (Fig.3(d)), where analogous results to Fig.2(d) are obtained. This demonstrates the capability of NHKPM to compute spectral functions and identify topological edge modes in the presence of NHSE. We note that in the presence of NHSE, bulk states become also localized at the edge. In this case, it is the definition of the local dynamical spin correlator in Eq. (4) that allows to distinguish edge states from bulk states, and image edge modes in real space. Another remark is that in the presence of NHSE, the condition number[58] of H increases exponentially. Therefore, numerically determining the exact spectrum of a Hamiltonian with NHSE is often very hard and time-consuming. In our algorithm, by using Eq.(7), this hard task is converted to the computation of the Green's function of a Hermitian Hamiltonian, which is relatively more controllable.

We now comment on several future perspectives for the NHKPM algorithm. It is worth noting that in some NH systems the physically relevant state could be the state with the largest imaginary energy, which is the steady state of the system after a long time evolution. The algo-

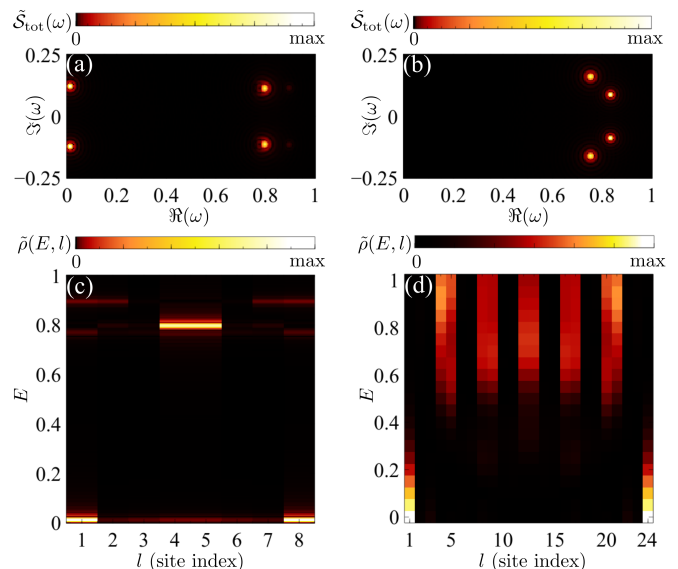


FIG. 3. (a,b) Total dynamical spin correlator $\tilde{S}_{\text{tot}}(\omega)$ of H defined in Eq. (9) with $L = 8$, $h_z = 2J$ and $\gamma = 0.1J$ under (a) open boundary condition and (b) periodic boundary condition. (c) Projected local dynamical structure factor $\tilde{\rho}(E, l)$ corresponding to (a), showing the persistence of topological end modes in the presence of NHSE. (d) $\tilde{\rho}(E, l)$ of H with $L = 24$, $h_z = J$ and $\gamma = 0.1J$, showing the topological end modes in the presence of NHSE for a longer chain.

gorithm could identify the energy of many-body excitations near that state, and applies efficiently as long as the state is not highly-entangled. In addition to addressing topology, the NHKPM algorithm can also address (higher-order) NHSE[59] by computing spectral functions defined in a basis of solely left (right) eigenvectors, or by computing the Green's function[60]. Finally, we note while our algorithm is implemented within the MPS formalism, this methodology can be extended to more generic tensor-network algorithms[61, 62] and neural-network quantum states[63, 64]. Such extensions would allow tackling many-body interacting two-dimensional non-Hermitian problems.

To summarize, we developed a NHKPM algorithm that can efficiently compute local spectral functions in a NH many-body model. In particular, we showed that this methodology allows to compute local dynamical spin correlators in a non-Hermitian interacting system featuring topological excitations, directly allowing to image the topological end modes in real and frequency space. We further showed that this algorithm works in the presence of the non-Hermitian skin effect. Our results put forward a new method to efficiently compute spectral functions of non-Hermitian many-body systems of large sizes beyond the capability of exact diagonalization, and make an essential step toward the critical open problem of addressing non-trivial topology in non-Hermitian many-body systems.

Acknowledgements We acknowledge the computational resources provided by the Aalto Science-IT project, and the financial support from the Academy of Finland Projects No. 331342 and No. 336243 and the Jane and Aatos Erkkö Foundation. We thank Z. Wang, S. Sayyad, T. Hyart, M. Niedermeier, and P. Vecsei for fruitful discussions. The numerical calculations are done with the ITensor library[65].

* songf18@mails.tsinghua.edu.cn

† jose.lado@aalto.fi

- [1] H. Breuer and F. Petruccione, *The Theory of Open Quantum Systems* (Oxford University Press, 2002).
- [2] E. J. Bergholtz, J. C. Budich, and F. K. Kunst, Exceptional topology of non-hermitian systems, *Rev. Mod. Phys.* **93**, 015005 (2021).
- [3] Y. Ashida, Z. Gong, and M. Ueda, Non-hermitian physics, *Advances in Physics* **69**, 249 (2020).
- [4] S. Yao and Z. Wang, Edge states and topological invariants of non-hermitian systems, *Phys. Rev. Lett.* **121**, 086803 (2018).
- [5] C. H. Lee and R. Thomale, Anatomy of skin modes and topology in non-hermitian systems, *Phys. Rev. B* **99**, 201103 (2019).
- [6] F. K. Kunst, E. Edvardsson, J. C. Budich, and E. J. Bergholtz, Biorthogonal bulk-boundary correspondence in non-hermitian systems, *Phys. Rev. Lett.* **121**, 026808 (2018).
- [7] L. Xiao, T. Deng, K. Wang, G. Zhu, Z. Wang, W. Yi, and P. Xue, Non-hermitian bulk-boundary correspondence in quantum dynamics, *Nature Physics* **16**, 761 (2020).
- [8] T. Helbig, T. Hofmann, S. Imhof, M. Abdelghany, T. Kiessling, L. W. Molenkamp, C. H. Lee, A. Szameit, M. Greiter, and R. Thomale, Generalized bulk-boundary correspondence in non-hermitian topoelectrical circuits, *Nature Physics* **16**, 747 (2020).
- [9] S. Weidemann, M. Kremer, T. Helbig, T. Hofmann, A. Stegmaier, M. Greiter, R. Thomale, and A. Szameit, Topological funneling of light, *Science* **368**, 311 (2020).
- [10] A. Ghatak, M. Brandenbourger, J. van Wezel, and C. Coulais, Observation of non-hermitian topology and its bulk-edge correspondence in an active mechanical metamaterial, *Proceedings of the National Academy of Sciences* **117**, 29561 (2020).
- [11] T. E. Lee, Anomalous edge state in a non-hermitian lattice, *Phys. Rev. Lett.* **116**, 133903 (2016).
- [12] V. M. Martinez Alvarez, J. E. Barrios Vargas, and L. E. F. Foa Torres, Non-hermitian robust edge states in one dimension: Anomalous localization and eigenspace condensation at exceptional points, *Phys. Rev. B* **97**, 121401 (2018).
- [13] Z. Gong, Y. Ashida, K. Kawabata, K. Takasan, S. Higashikawa, and M. Ueda, Topological phases of non-hermitian systems, *Phys. Rev. X* **8**, 031079 (2018).
- [14] K. Kawabata, K. Shiozaki, M. Ueda, and M. Sato, Symmetry and topology in non-hermitian physics, *Phys. Rev. X* **9**, 041015 (2019).
- [15] H. Zhou and J. Y. Lee, Periodic table for topological bands with non-hermitian symmetries, *Phys. Rev. B* **99**, 235112 (2019).
- [16] N. Okuma, K. Kawabata, K. Shiozaki, and M. Sato, Topological origin of non-hermitian skin effects, *Phys. Rev. Lett.* **124**, 086801 (2020).
- [17] K. Zhang, Z. Yang, and C. Fang, Correspondence between winding numbers and skin modes in non-hermitian systems, *Phys. Rev. Lett.* **125**, 126402 (2020).
- [18] D. S. Borgnia, A. J. Kruchkov, and R.-J. Slager, Non-hermitian boundary modes and topology, *Phys. Rev. Lett.* **124**, 056802 (2020).
- [19] C. M. Bender and S. Boettcher, Real spectra in non-hermitian hamiltonians having pt symmetry, *Phys. Rev. Lett.* **80**, 5243 (1998).
- [20] C. M. Bender, Making sense of non-hermitian hamiltonians, *Reports on Progress in Physics* **70**, 947 (2007).
- [21] R. El-Ganainy, K. G. Makris, M. Khajavikhan, Z. H. Musslimani, S. Rotter, and D. N. Christodoulides, Non-hermitian physics and pt symmetry, *Nature Physics* **14**, 11 (2018).
- [22] W. D. Heiss, Exceptional points of non-hermitian operators, *Journal of Physics A: Mathematical and General* **37**, 2455 (2004).
- [23] M. V. Berry, Physics of nonhermitian degeneracies, *Czechoslovak journal of physics* **54**, 1039 (2004).
- [24] M.-A. Miri and A. Alù, Exceptional points in optics and photonics, *Science* **363**, 10.1126/science.aar7709 (2019).
- [25] Ş. K. Özdemir, S. Rotter, F. Nori, and L. Yang, Parity-time symmetry and exceptional points in photonics, *Nature Materials* **18**, 783 (2019).
- [26] S.-B. Zhang, M. M. Denner, T. c. v. Bzdušek, M. A. Sentef, and T. Neupert, Symmetry breaking and spectral structure of the interacting hatano-nelson model, *Phys. Rev. B* **106**, L121102 (2022).
- [27] D. J. Luitz and F. Piazza, Exceptional points and the topology of quantum many-body spectra, *Phys. Rev. Research* **1**, 033051 (2019).
- [28] R. Schäfer, J. C. Budich, and D. J. Luitz, Symmetry protected exceptional points of interacting fermions (2022), [arXiv:2204.05340 \[quant-ph\]](https://arxiv.org/abs/2204.05340).
- [29] K. Kawabata, K. Shiozaki, and S. Ryu, Many-body topology of non-hermitian systems, *Phys. Rev. B* **105**, 165137 (2022).
- [30] F. Alsallom, L. Herviou, O. V. Yazyev, and M. Brzezińska, Fate of the non-hermitian skin effect in many-body fermionic systems, *Phys. Rev. Research* **4**, 033122 (2022).
- [31] S. R. White, Density matrix formulation for quantum renormalization groups, *Phys. Rev. Lett.* **69**, 2863 (1992).
- [32] T. D. Kühner and S. R. White, Dynamical correlation functions using the density matrix renormalization group, *Phys. Rev. B* **60**, 335 (1999).
- [33] E. Jeckelmann, Dynamical density-matrix renormalization-group method, *Phys. Rev. B* **66**, 045114 (2002).
- [34] S. R. White and A. E. Feiguin, Real-time evolution using the density matrix renormalization group, *Phys. Rev. Lett.* **93**, 076401 (2004).
- [35] J. Haegeman, J. I. Cirac, T. J. Osborne, I. Pižorn, H. Verschelde, and F. Verstraete, Time-dependent variational principle for quantum lattices, *Phys. Rev. Lett.* **107**, 070601 (2011).
- [36] A. Weiße, G. Wellein, A. Alvermann, and H. Fehske, The kernel polynomial method, *Rev. Mod. Phys.* **78**, 275

- (2006).
- [37] F. A. Wolf, I. P. McCulloch, O. Parcollet, and U. Schollwöck, Chebyshev matrix product state impurity solver for dynamical mean-field theory, *Phys. Rev. B* **90**, 115124 (2014).
- [38] J. L. Lado and O. Zilberberg, Topological spin excitations in harper-heisenberg spin chains, *Phys. Rev. Research* **1**, 033009 (2019).
- [39] N. Hatano and J. Feinberg, Chebyshev-polynomial expansion of the localization length of hermitian and non-hermitian random chains, *Phys. Rev. E* **94**, 063305 (2016).
- [40] The source codes are available on <https://github.com/GUANGZECHEN/NHKPM.jl>.
- [41] A. J. Heinrich, J. A. Gupta, C. P. Lutz, and D. M. Eigler, Single-atom spin-flip spectroscopy, *Science* **306**, 466–469 (2004).
- [42] A. Spinelli, B. Bryant, F. Delgado, J. Fernández-Rossier, and A. F. Otte, Imaging of spin waves in atomically designed nanomagnets, *Nature Materials* **13**, 782–785 (2014).
- [43] S. Baumann, W. Paul, T. Choi, C. P. Lutz, A. Ardavan, and A. J. Heinrich, Electron paramagnetic resonance of individual atoms on a surface, *Science* **350**, 417–420 (2015).
- [44] K. Yang, Y. Bae, W. Paul, F. D. Natterer, P. Willke, J. L. Lado, A. Ferrón, T. Choi, J. Fernández-Rossier, A. J. Heinrich, and C. P. Lutz, Engineering the eigenstates of coupled spin-1/2 atoms on a surface, *Phys. Rev. Lett.* **119**, 227206 (2017).
- [45] S. Kezilebieke, R. Žitko, M. Dvorak, T. Ojanen, and P. Liljeroth, Observation of coexistence of yu-shiba-rusinov states and spin-flip excitations, *Nano Letters* **19**, 4614–4619 (2019).
- [46] S.-B. Zhang, M. M. Denner, T. Bzdušek, M. A. Sentef, and T. Neupert, Symmetry breaking and spectral structure of the interacting hatano-nelson model (2022), [arXiv:2201.12653](https://arxiv.org/abs/2201.12653).
- [47] There exists a multi-variable Chebyshev expansion for $f(\omega)$, yet the coefficients in such case cannot be computed efficiently as in Eq. (3)[36].
- [48] See Supplemental Material for the technical details of our algorithm and the analysis of the numerical complexity of our algorithm. Refs.[66–72] are included in the Supplemental Material.
- [49] J. Feinberg and A. Zee, Non-hermitian random matrix theory: Method of hermitian reduction, *Nuclear Physics B* **504**, 579 (1997).
- [50] G. W. Stewart, A krylov–schur algorithm for large eigenproblems, *SIAM Journal on Matrix Analysis and Applications* **23**, 601 (2002).
- [51] The fidelity of these states are verified in the Supplemental Material.
- [52] W. Brzezicki and T. Hyart, Hidden chern number in one-dimensional non-hermitian chiral-symmetric systems, *Phys. Rev. B* **100**, 161105 (2019).
- [53] K. Kawabata, K. Shiozaki, M. Ueda, and M. Sato, Symmetry and topology in non-hermitian physics, *Phys. Rev. X* **9**, 041015 (2019).
- [54] T. Hyart and J. L. Lado, Non-hermitian many-body topological excitations in interacting quantum dots, *Phys. Rev. Research* **4**, L012006 (2022).
- [55] We take the absolute value in Eq. (11) since $\mathcal{S}(\omega, l)$ is no longer real-valued in this case.
- [56] L. Herviou, J. H. Bardarson, and N. Regnault, Defining a bulk-edge correspondence for non-hermitian hamiltonians via singular-value decomposition, *Phys. Rev. A* **99**, 052118 (2019).
- [57] We demonstrate this with the Hatano-Nelson model[73] in the Supplemental Material.
- [58] D. Belsley, E. Kuh, and R. Welsch, *Regression Diagnostics: Identifying Influential Data and Sources of Collinearity*, Wiley Series in Probability and Statistics (Wiley, 2005).
- [59] K. Kawabata, M. Sato, and K. Shiozaki, Higher-order non-hermitian skin effect, *Phys. Rev. B* **102**, 205118 (2020).
- [60] W.-T. Xue, M.-R. Li, Y.-M. Hu, F. Song, and Z. Wang, Simple formulas of directional amplification from non-bloch band theory, *Phys. Rev. B* **103**, L241408 (2021).
- [61] J. I. Cirac, D. Pérez-García, N. Schuch, and F. Verstraete, Matrix product states and projected entangled pair states: Concepts, symmetries, theorems, *Rev. Mod. Phys.* **93**, 045003 (2021).
- [62] R. Orús, A practical introduction to tensor networks: Matrix product states and projected entangled pair states, *Annals of Physics* **349**, 117–158 (2014).
- [63] G. Carleo and M. Troyer, Solving the quantum many-body problem with artificial neural networks, *Science* **355**, 602–606 (2017).
- [64] D. Hendry, H. Chen, P. Weinberg, and A. E. Feiguin, Chebyshev expansion of spectral functions using restricted boltzmann machines, *Phys. Rev. B* **104**, 205130 (2021).
- [65] M. Fishman, S. R. White, and E. M. Stoudenmire, The ITensor software library for tensor network calculations (2020), [arXiv:2007.14822](https://arxiv.org/abs/2007.14822).
- [66] H. G. Dawson, On the numerical value of $\int_0^h \exp(x^2)dx$, *Proceedings of the London Mathematical Society* **s1-29**, 519 (1897).
- [67] N. Okuma and M. Sato, Hermitian zero modes protected by nonnormality: Application of pseudospectra, *Phys. Rev. B* **102**, 014203 (2020).
- [68] U. Schollwöck, The density-matrix renormalization group in the age of matrix product states, *Annals of Physics* **326**, 96 (2011), january 2011 Special Issue.
- [69] T. Enss and U. Schollwöck, On the choice of the density matrix in the stochastic tmrg, *Journal of Physics A: Mathematical and General* **34**, 7769 (2001).
- [70] G. K.-L. Chan and T. Van Voorhis, Density-matrix renormalization-group algorithms with nonorthogonal orbitals and non-hermitian operators, and applications to polyenes, *The Journal of Chemical Physics* **122**, 204101 (2005).
- [71] D.-W. Zhang, Y.-L. Chen, G.-Q. Zhang, L.-J. Lang, Z. Li, and S.-L. Zhu, Skin superfluid, topological mott insulators, and asymmetric dynamics in an interacting non-hermitian aubry-andré-harper model, *Phys. Rev. B* **101**, 235150 (2020).
- [72] K. Yamamoto, M. Nakagawa, M. Tezuka, M. Ueda, and N. Kawakami, Universal properties of dissipative tomonaga-luttinger liquids: Case study of a non-hermitian xxz spin chain, *Phys. Rev. B* **105**, 205125 (2022).
- [73] N. Hatano and D. R. Nelson, Localization transitions in non-hermitian quantum mechanics, *Phys. Rev. Lett.* **77**, 570 (1996).

Supplemental Material for “Topological spin excitations in non-Hermitian spin chains with a generalized kernel polynomial algorithm”

Guangze Chen,¹ Fei Song,^{2,*} and Jose L. Lado^{1,†}

¹*Department of Applied Physics, Aalto University, 02150 Espoo, Finland*
²*Institute for Advanced Study, Tsinghua University, Beijing, 100084, China*

(Dated: March 10, 2023)

DETAILS OF THE NHKPM METHOD

We derived in the main text that the spectral function

$$f(\omega) = \langle \psi_L | \delta^2(\omega - H) | \psi_R \rangle \quad (\text{S1})$$

can be computed with

$$f(\omega) = \frac{1}{\pi} \partial_{\omega^*} G(E=0) \quad (\text{S2})$$

where

$$G(E) = \langle L | (E - \mathcal{H})^{-1} | R \rangle \quad (\text{S3})$$

is an entry of the Green’s function of the Hermitrized Hamiltonian \mathcal{H} (Eq. (6) in the main text) with

$$|L\rangle = \begin{pmatrix} 0 \\ |\psi_L\rangle \end{pmatrix}, |R\rangle = \begin{pmatrix} |\psi_R\rangle \\ 0 \end{pmatrix}. \quad (\text{S4})$$

Since $G(E)$ is a function of a single variable, we can apply KPM to compute $G(E)$, let

$$G(E) = B(E) - iA(E), \quad (\text{S5})$$

where $A(E) = \langle L | \delta(E - \mathcal{H}) | R \rangle$ and $B(E)$ is its Hilbert transform:

$$B(E) = \frac{1}{\pi} \mathcal{P} \int_{-\infty}^{\infty} dE' \frac{A(E')}{E - E'}, \quad (\text{S6})$$

where \mathcal{P} denotes the Cauchy principal value. Performing a scaling on \mathcal{H} : $\mathcal{H} \rightarrow \mathcal{H}/\Delta$ such that its spectrum lies in $(-1, 1)$, we can perform a Chebyshev expansion on $A(E)$ [1]:

$$A(E) = \frac{1}{\pi\sqrt{1-E^2}} \left(\mu_0 + 2 \sum_{n=1}^{\infty} \mu_n T_n(E) \right), \quad (\text{S7})$$

where

$$\mu_n = \int_{-1}^1 dE A(E) T_n(E) = \langle L | T_n(\mathcal{H}) | R \rangle, \quad (\text{S8})$$

and $T_n(x) = \cos(n \arccos x)$ satisfying the following recursion relation:

$$\begin{aligned} T_0(x) &= 1, T_1(x) = x, \\ T_{n+1}(x) &= 2xT_n(x) - T_{n-1}(x). \end{aligned} \quad (\text{S9})$$

Using

$$\mathcal{P} \int_{-1}^1 \frac{T_n(y) dy}{(y-x)\sqrt{1-y^2}} = \pi U_{n-1}(x), \quad (\text{S10})$$

together with Eqs. (S6) and (S7), we have

$$B(E) = \frac{2}{\pi} \sum_{n=1}^{\infty} \mu_n U_{n-1}(E) \quad (\text{S11})$$

where $U_n(x) = \sin[(n+1) \arccos x] / \sin[\arccos x]$. Combining Eqs. (S5), (S7) and (S11), we have

$$G(E=0) = \frac{2}{\pi} \sum_{n=1}^{\infty} (-1)^{n+1} \mu_{2n-1}, \quad (\text{S12})$$

which can be computed by noting that $\mu_n = 0$ for even n and $T_n(0) = U_n(0) = 0$ for odd n . Combining Eq. (S2), Eq. (S8) and Eq. (S12), we have Eq. (8) in the main text:

$$f(\omega) = \frac{2}{\pi^2} \sum_{n=1}^{\infty} (-1)^{n+1} \langle L | \partial_{\omega^*} T_{2n-1}(\mathcal{H}) | R \rangle, \quad (\text{S13})$$

with the recursion relation

$$\begin{aligned} \partial_{\omega^*} T_{n+1}(\mathcal{H}) &= 2 \begin{pmatrix} 0 \\ 1 \end{pmatrix} T_n(\mathcal{H}) \\ &\quad + 2\mathcal{H} \partial_{\omega^*} T_n(\mathcal{H}) - \partial_{\omega^*} T_{n-1}(\mathcal{H}). \end{aligned} \quad (\text{S14})$$

We now elaborate on the numerical details in the computation of $f(\omega)$. Let

$$|A_n\rangle = T_n(\mathcal{H}) | R \rangle \quad (\text{S15})$$

and

$$|\Psi_n\rangle = \partial_{\omega^*} T_n(\mathcal{H}) | R \rangle. \quad (\text{S16})$$

We can verify that

$$\begin{aligned} |A_0\rangle &= \begin{pmatrix} |\psi_R\rangle \\ 0 \end{pmatrix}, |A_1\rangle = \begin{pmatrix} 0 \\ (\omega^* - H^\dagger) |\psi_R\rangle \end{pmatrix} \\ |\Psi_0\rangle &= \begin{pmatrix} 0 \\ 0 \end{pmatrix}, |\Psi_1\rangle = \begin{pmatrix} 0 \\ |\psi_R\rangle \end{pmatrix} \end{aligned} \quad (\text{S17})$$

with recursion relation

$$\begin{aligned} |A_{n+1}\rangle &= 2\mathcal{H}|A_n\rangle - |A_{n-1}\rangle \\ |\Psi_{n+1}\rangle &= 2 \begin{pmatrix} 0 \\ 1 \end{pmatrix} |A_n\rangle + 2\mathcal{H}|\Psi_n\rangle - |\Psi_{n-1}\rangle. \end{aligned} \quad (\text{S18})$$

Let

$$\begin{aligned} |A_{2n}\rangle &= \begin{pmatrix} |\alpha_{2n}\rangle \\ 0 \end{pmatrix}, |A_{2n+1}\rangle = \begin{pmatrix} 0 \\ |\alpha_{2n+1}\rangle \end{pmatrix} \\ |\Psi_{2n}\rangle &= \begin{pmatrix} |\psi_{2n}\rangle \\ 0 \end{pmatrix}, |\Psi_{2n+1}\rangle = \begin{pmatrix} 0 \\ |\psi_{2n+1}\rangle \end{pmatrix} \end{aligned} \quad (\text{S19})$$

where $n \in \mathbb{Z}$ and $n \geq 0$. We thus arrive at the following recursion relation

$$\begin{aligned} |\alpha_{2n}\rangle &= 2(\omega - H)|\alpha_{2n-1}\rangle - |\alpha_{2n-2}\rangle \\ |\alpha_{2n+1}\rangle &= 2(\omega^* - H^\dagger)|\alpha_{2n}\rangle - |\alpha_{2n-1}\rangle \\ |\psi_{2n}\rangle &= 2(\omega - H)|\psi_{2n-1}\rangle - |\psi_{2n-2}\rangle \\ |\psi_{2n+1}\rangle &= 2|\alpha_{2n}\rangle + 2(\omega^* - H^\dagger)|\psi_{2n}\rangle - |\psi_{2n-1}\rangle \end{aligned} \quad (\text{S20})$$

with

$$\begin{aligned} |\alpha_0\rangle &= |\psi_R\rangle, |\alpha_1\rangle = (\omega^* - H^\dagger)|\psi_R\rangle \\ |\psi_0\rangle &= 0, |\psi_1\rangle = |\psi_R\rangle, \end{aligned} \quad (\text{S21})$$

and Eq.(S13) becomes

$$f(\omega) = \frac{2}{\pi^2} \sum_{n=1}^{\infty} (-1)^{n+1} \langle \psi_L | \psi_{2n-1} \rangle. \quad (\text{S22})$$

In practice, we do a truncation of Eq. (S22) to order N :

$$f_{\text{KPM}}(\omega) = \frac{2}{\pi^2} \sum_{n=1}^N (-1)^{n+1} g_{2n-1}^{2N} \langle \psi_L | \psi_{2n-1} \rangle. \quad (\text{S23})$$

where

$$g_n^{2N} = \frac{(2N - n + 1) \cos \frac{n\pi}{2N+1} + \sin \frac{n\pi}{2N+1} \cot \frac{\pi}{2N+1}}{2N + 1} \quad (\text{S24})$$

is the Jackson kernel to suppress Gibbs oscillations and improve the accuracy[2]. We note that Eq. (S23) can also be written as:

$$f_{\text{KPM}}(\omega) = \frac{1}{\pi} \partial_{\omega^*} G_{\text{KPM}}(E = 0) \quad (\text{S25})$$

where

$$G_{\text{KPM}}(E = 0) = \frac{2}{\pi} \sum_{n=1}^N (-1)^{n+1} g_{2n-1} \mu_{2n-1} \quad (\text{S26})$$

is a finite-series approximation to Eq. (S12) with the Jackson kernel g_n . The truncation to the N^{th} order polynomial with a Jackson kernel is known to provide a Gaussian approximation to the Dirac delta function[2]:

$$(\delta(x))_{\text{Jackson}} \approx \frac{1}{\sqrt{2\pi\sigma^2}} e^{-\frac{x^2}{2\sigma^2}}, \quad (\text{S27})$$

where $\sigma = \pi/N$. Performing a Hilbert transform on both sides of Eq. (S27), we have:

$$\left(\frac{1}{x}\right)_{\text{Jackson}} \approx \frac{2}{\sqrt{2\sigma^2}} F\left(\frac{x}{\sqrt{2\sigma^2}}\right) \quad (\text{S28})$$

where $F(x) = \exp(-x^2) \int_0^x \exp(t^2) dt$ is the Dawson function[3]. Eq. (S28) provides a good approximation for $1/x$ for $x \gtrsim 2\sigma$. Now, for $G(E = 0)$, the KPM procedure provides an approximation:

$$\begin{aligned} G(E = 0) &= -\langle L | \mathcal{H}^{-1} | R \rangle \\ &= -\sum_n \langle L | \varphi_n \rangle \mathcal{E}_n^{-1} \langle \varphi_n | R \rangle \\ &\approx -\sum_n \langle L | \varphi_n \rangle (\mathcal{E}_n^{-1})_{\text{Jackson}} \langle \varphi_n | R \rangle, \end{aligned} \quad (\text{S29})$$

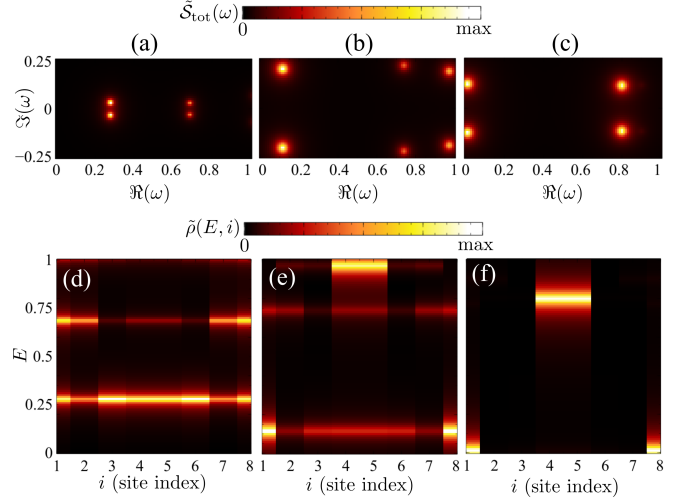


FIG. S1. Spectral functions in Fig.1 in the main text, computed with exact diagonalization.

where \mathcal{E}_n and $|\varphi_n\rangle$ are the eigen-decomposition of \mathcal{H} . Eq. (S29) is a good approximation as long as

$$\sigma \lesssim \frac{\min(\mathcal{E}_n)}{2\Delta}, \quad (\text{S30})$$

where Δ is the factor we divide \mathcal{H} with to keep its spectrum in $(-1, 1)$. A sufficiently small σ can be achieved by increasing N in our computation.

Due to the derivative in Eq. (S2), a quantitative analysis of the approximation we did for $f(\omega)$ is difficult. Qualitatively, delta functions in $f(\omega)$ are smeared in $f_{\text{KPM}}(\omega)$ with a width $d \approx \frac{\pi\Delta}{N}$, where Δ is the scaling factor to \mathcal{H} to make its spectrum in $(-1, 1)$. For $L = 8$, $\Delta = 6$ is sufficient in our computation, and for $L = 24$, we take $\Delta = 16$.

For $L = 8$, the low-energy spectra computed with NHKPM agree with results obtained with exact diagonalization (ED) qualitatively (Fig.S1). An exact correspondence does not exist here since in ED the delta function is approximated with a Gaussian, whereas with NHKPM it is approximated with another peaked function as discussed above.

TOTAL DENSITY OF STATES IN HATANO-NELSON MODEL WITH NHKPM

To show that the NHKPM faithfully computes spectral functions in the single particle case in the presence of non-Hermitian skin effect (NHSE), we consider the Hatano-Nelson model[4]:

$$H_{\text{HN}} = \sum_{l=1}^{L-1} (t + \gamma) c_l^\dagger c_{l+1} + (t - \gamma) c_{l+1}^\dagger c_l, \quad (\text{S31})$$

which exhibits NHSE when $\gamma \neq 0$. We compute the total density of states of the model:

$$\rho_{\text{tot}}(\omega) = \sum_n \delta(\Re(\omega - E_n))\delta(\Im(\omega - E_n)). \quad (\text{S32})$$

For simplicity we take $L = 8$, and we note that analogous results can be obtained for larger L . The spectrum of H_{HN} computed with ED with $t = 1$ and $\gamma = 0.4$ under periodic boundary condition (PBC) and open boundary condition (OBC) are shown in Figs.S2(a) and (d). We see that the PBC spectrum features a point gap, whereas the OBC spectrum is purely real. The spectrum computed with NHKPM in both cases are shown in Figs.S2(b) and (e), demonstrating the capability of NHKPM to provide faithful results in both cases. As discussed in the main text, the reason that NHKPM provides a faithful OBC spectrum in this case is due to the contribution of the zero modes of \mathcal{H} to $G(E = 0)$ when ω lies in the point gap of H . Due to finite-size effects, these zero modes have an exponentially small finite energy: $\mathcal{E}_0 \propto \exp(-L/L_0)$ where L_0 is a constant. According to Eq. (S30), to accurately capture the contribution of this zero mode to $G(E = 0)$, we require:

$$\sigma = \frac{\pi}{N} \lesssim \frac{\mathcal{E}_0}{2\Delta}, \quad (\text{S33})$$

which for the exponentially small \mathcal{E}_0 requires an exponentially large N , hence the large N in Figs.S2(e). When smaller N is used, the computed spectrum becomes a pseudo-spectrum[5] under OBC (Fig.S2(f)) due to inaccurately accounting for the contribution of the zero mode to $G(E = 0)$, while the spectrum under PBC only gets broadened (Fig.S2(c)). For comparison we also show the OBC spectrum computed with $\gamma = 0$ (Fig.S2(g-i)), where only a broadening is observed for smaller N due to the absence of NHSE.

ENTANGLEMENT ENTROPY GROWTH DURING THE RECURSIVE CALCULATIONS

The updating of the states $|\psi_n\rangle$ in Eq. (S20) can result in states with large entanglement for large n even if the initial state $|\psi_{\text{R}}\rangle$ is not much entangled. A largely entangled state would require larger bond dimensions in the matrix-product state (MPS) representation of the states, which increases computational cost. We analyze this entanglement increase in our calculation of the spectral function Eq.(4) for the Hamiltonian Eq.(9) in the main text, and we focus on the case $L = 24$. For concreteness we choose $|\psi_{\text{L,R}}\rangle = S_l^x |\text{GS}_{\text{L,R}}\rangle$ with $l = 12$, and the choice of ω is different in each specific case. We note that the results are qualitatively independent of the choice of site index l and ω .

The entanglement of a certain state $|\psi\rangle$ is characterized by the entanglement entropy at the middle of the chain

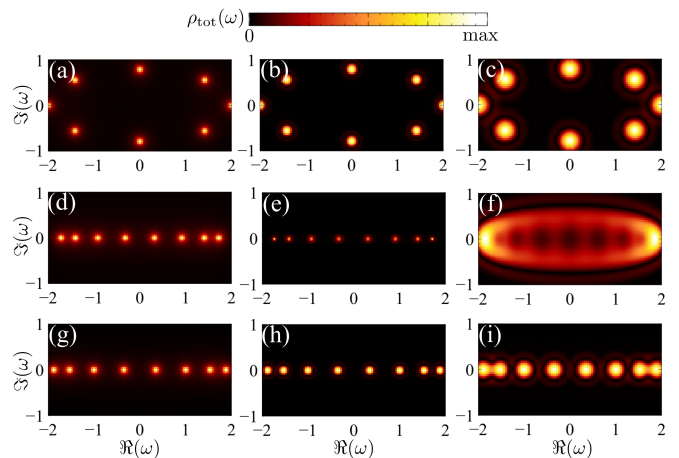


FIG. S2. Total density of states $\rho_{\text{tot}}(\omega)$ defined in Eq. (S32) for H_{HN} with $L = 8$ and $t = 1$, with (a) $\gamma = 0.4$, under PBC, computed with ED, (b) $\gamma = 0.4$, under PBC, computed with NHKPM with $N = 100$, (c) $\gamma = 0.4$, under PBC, computed with NHKPM with $N = 50$, (d) $\gamma = 0.4$, under OBC, computed with ED, (e) $\gamma = 0.4$, under OBC, computed with NHKPM with $N = 1000$, (f) $\gamma = 0.4$, under OBC, computed with NHKPM with $N = 50$, (g) $\gamma = 0$, under OBC, computed with ED, (h) $\gamma = 0$, under OBC, computed with NHKPM with $N = 100$, and (i) $\gamma = 0$, under OBC, computed with NHKPM with $N = 50$.

S_{ent} , defined as

$$S_{\text{ent}}(|\psi\rangle) = \text{Tr}(\rho_A \log \rho_A) \quad (\text{S34})$$

$$\rho_A = \text{Tr}_B(|\psi\rangle\langle\psi|), \quad (\text{S35})$$

where A and B are the left half and right half of the chain. The entanglement entropy defined in this way is meant to measure the numerical complexity to capture the wavefunction. In particular, for an MPS, it provides a lower bound for the bond dimension m [6]:

$$S_{\text{ent}} \leq S_{\text{max}} = - \sum_{i=1}^m \frac{1}{m} \log_2\left(\frac{1}{m}\right) = \log_2 m, \quad (\text{S36})$$

where S_{max} is the largest possible entanglement entropy of a bond of dimension m . Thus, a larger S_{ent} indicates that a larger bond dimension is needed to accurately represent the state with MPS.

We first analyze S_{ent} for $|\psi_n\rangle$ in the Hermitian case, and with different bond dimensions m used in the MPS representation (Fig.S3(a)). It is first observed that for $m = 50$ and $m = 100$ the entanglement entropy starts to differ from results computed with a higher bond dimension at around $n = 500$, indicating that m is too small to accurately represent the state. Another observation is that the entanglement entropy saturates to a small value around 2 for large n , allowing the states to be represented accurately using a small m . As a consequence, the coefficients μ_{2n-1} computed with $m = 200$ is accurate up to $n = 600$, and with $m = 300$ is accurate up to

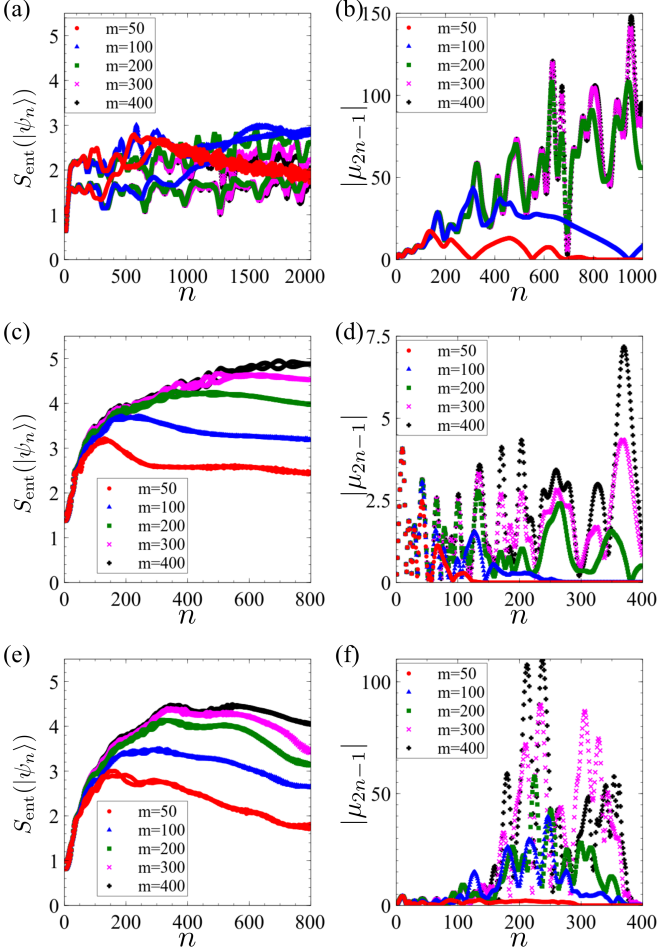


FIG. S3. (a) Entanglement entropy of $|\psi_n\rangle$ and (b) the coefficients $|\mu_{2n-1}|$ in the iterative calculation Eq. (S20) for H in Eq. (9) in main text with $h_z = \gamma = 0$ and $\omega = 0.1$. (c,d) Same as (a,b), but with $h_z = J$, $\gamma = 0$ and $\omega = 0.23i$. (e,f) Same as (a,b), but with $h_z = J$, $\gamma = 0.1J$ and $\omega = 0.23i$.

$n = 1000$ (Fig.S3(b)). When a large non-Hermitian term $h_z = J$ is considered, the entanglement increase in the iterations becomes faster, and the entanglement entropy grows to a much larger value compared to the Hermitian case (Fig.S3(c)). As a consequence, the number of faithful coefficients drops for the same bond dimension m used (Fig.S3(d)). In the Hermitian case, Figs.2(a,c) in the main text are computed with $N = 500$ and $m = 200$. In the case $h_z = J$, Figs.2(b,d) in the main text are computed with $N = 300$ and $m = 300$.

The presence of the non-Hermitian skin effect also results in a faster increase of entanglement entropy of $|\psi_n\rangle$ (Fig.S3(e)), and the faithful number of coefficients for fixed m further drops (Fig.S3(f)). As a consequence, Fig.3(d) in the main text is computed with $N = 200$ and $m = 400$.

NUMERICAL COMPLEXITY OF NHKPM

We analyze the numerical complexity of our algorithm in this section. In essence, an optimized version of our algorithm scales approximately as L^3 , with L the number of sites. This power law dependence makes our algorithm scalable to bigger systems. We elaborate on the details below.

We analyze the time consumption to compute the spectral function (Eq.(4) in the main text):

$$\mathcal{S}(\omega, l) = \langle \text{GS}_L | S_l^- \delta^2(\omega + E_{\text{GS}} - H) S_l^+ | \text{GS}_R \rangle + \langle \text{GS}_L | S_l^+ \delta^2(\omega + E_{\text{GS}} - H) S_l^- | \text{GS}_R \rangle \quad (\text{S37})$$

with NHKPM for different system size L , where H and $|\text{GS}_{L,R}\rangle$ are given. In our particular case, the Hamiltonian H is given by Eq.(9) in the main text, and $|\text{GS}_{L,R}\rangle$ are computed with the Krylov-Schur algorithm. We focus on the topologically non-trivial regime: $h_z = J$, $\gamma = 0$, and fix $\omega = 0.23i$ and $l = 1$ as the spectral function shows a peak at this point due to the topological edge excitations. We note that the energy mesh and a sweep over all sites required to compute the full spectral function can be easily parallelized. As a result, the scaling of the algorithm is determined by the size dependence for a fixed ω and l .

We fix the broadening of the peak for the scaling analysis. As the system size increases, a larger scaling factor Δ is required to scale the spectrum of \mathcal{H} into $(-1, 1)$. Thus, to ensure the same broadening, the number of polynomials N should correspondingly increase. For our specific model, Δ is proportional to L , and thus we choose $N \propto L$ for the scaling analysis.

We first analyze the scaling of our algorithm for a generic case where the bond dimension of the MPS m is fixed. In this case, the time consumption shows an approximately 3rd power dependence on the system size (Fig.S4(a)). This scaling is the same as the kernel polynomial algorithm for Hermitian interacting systems[7].

We also analyze the scaling for our specific computation, where the entanglement entropy of states increases during the recursive calculations in the kernel polynomial method. In this case, to ensure the computational accuracy, a sufficiently large m is required, which increases with L . In Fig.S5, we show the computed spectral functions as a function of m for different sizes L . We show this for both $\omega = 0.23i$ where the spectral function is dominated at the boundary, and for $\omega = 0.8$ where the spectral function is dominated in the bulk. We observe that as m increases, the computed spectral function approaches the accurate value as expected. We also observe that although the accuracy is low for small m , it is still clear that for $\omega = 0.23i$ there exist edge excitations, and for $\omega = 0.8$ the excitations are more distributed in the bulk. Thus, a relative error of 10% is sufficient for the characterization of topological edge states. The small-

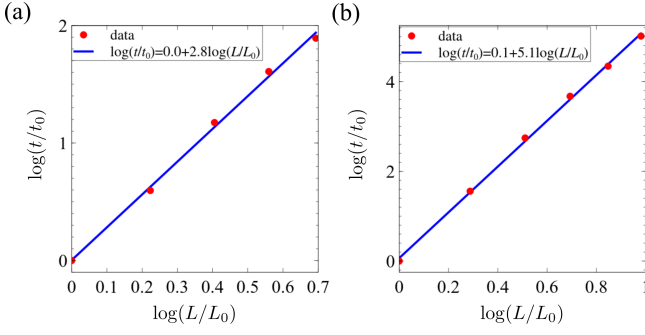


FIG. S4. (a) Complexity of NHKPM algorithm with fixed bond dimension $m = 80$ in MPS computations and $N = 25L/2$, with $L_0 = 16$ and $t_0 = 442.9\text{s}^{\text{a}}$. The log-log data is fitted with a linear function, indicating that the complexity of the algorithm is power-law with $(t/t_0) \propto (L/L_0)^{2.8}$. (b) Complexity of NHKPM algorithm with bond dimension $m = 10L/3$ in MPS computations and $N = 25L/2$, with $L_0 = 12$ and $t_0 = 30.4\text{s}^{\text{b}}$. The log-log fit indicates a power-law complexity with $(t/t_0) \propto (L/L_0)^5$.

^a The data is obtained with the Julia @btimes function, which averages time consumption over several computations. The computations are done on [Aalto University's triton cluster node pe84](#), with the CPU Intel Xeon E5 2680 v4.

^b The computations are done on [Aalto University's triton cluster node c604](#), with the CPU Intel Xeon E5 2690 v3.

est m required for this accuracy is $m = 40, 50, 60, 80$ for $L = 12, 16, 20, 24$, respectively. For simplicity, we choose $m = 10L/3$ to study the scaling, resulting in computational time $t \propto L^5$ (Fig.S4(b)). Compared to the fixed m case, the additional power of 2 originates from the fact that the complexity of applying a matrix product operator (MPO) on an MPS is proportional to m^2 , and we have used $m \propto L$ in this case.

FIDELITY OF GROUND STATES COMPUTED WITH THE KRYLOV-SCHUR ALGORITHM

The ground states are computed with the Krylov-Schur algorithm[8] in our case using matrix product state algebra. This method relies on an iterative algorithm to find the Krylov subspace expanded by a set of matrix-product states. Compared to generalized DMRG algorithms[9–12], this method does not have the limitations given by the local updates of DMRG-like sweeps, and its accuracy is solely controlled by the bond dimension. In addition, it applies to arbitrary Hamiltonians without requiring specific symmetries, which is beneficial for studying Hamiltonians with generic ground states as in the case we studied.

We first compute the Krylov space expanded by 4 eigenvectors with the smallest real eigenvalue. We then identify the one with the smallest real eigenvalue out of the 4 as the ground state. In this way, we avoid the risk of mistaking an eigenvector with a similar eigenvalue to the

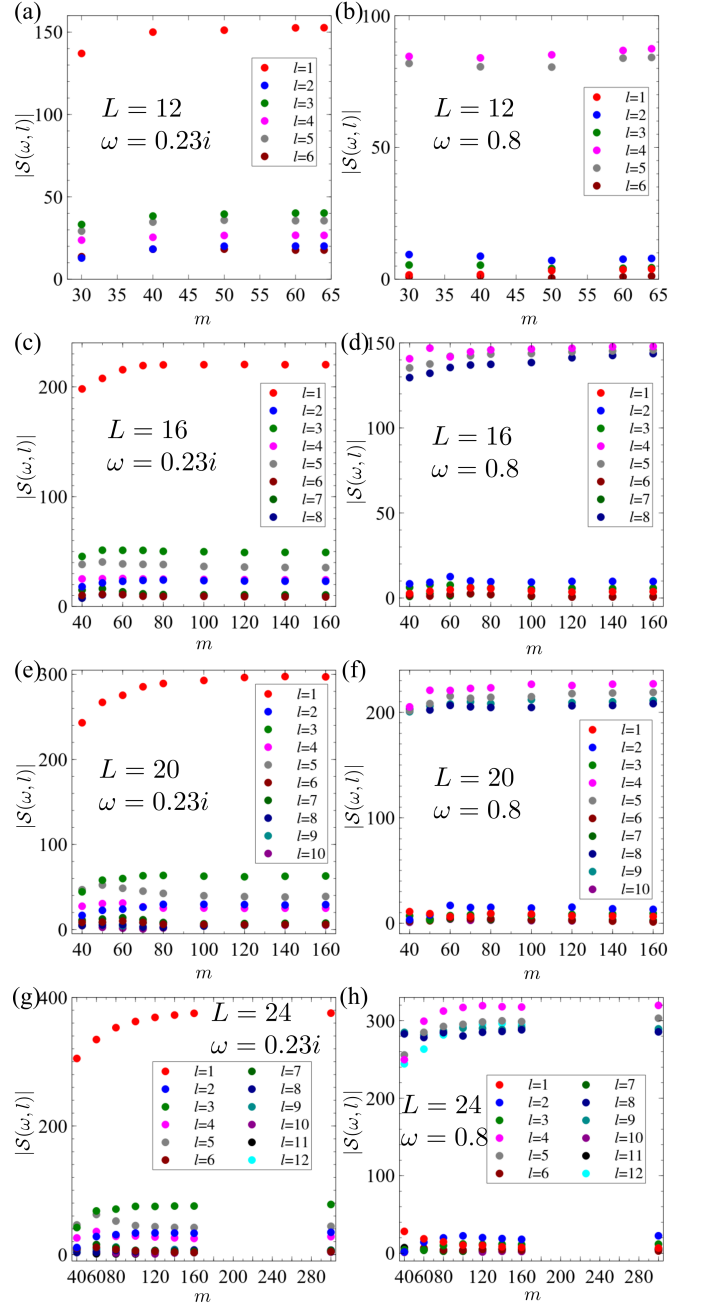


FIG. S5. The spectral function $\mathcal{S}(\omega, l)$ computed for different L and ω as a function of maximum bond dimension m . The parameters for H (Eq. (9) in the main text) are $h_z = J$ and $\gamma = 0$.

ground state as the ground state. The calculated ground state is then verified by checking the deviations:

$$d_{\text{R}}(|\psi_{\text{R}}\rangle) = \frac{|\langle \psi_{\text{R}} | H^\dagger H | \psi_{\text{R}} \rangle| - |\langle \psi_{\text{R}} | H | \psi_{\text{R}} \rangle|^2}{|\langle \psi_{\text{R}} | H^\dagger H | \psi_{\text{R}} \rangle|} \quad (\text{S38})$$

$$d_{\text{L}}(|\psi_{\text{L}}\rangle) = \frac{|\langle \psi_{\text{L}} | H H^\dagger | \psi_{\text{L}} \rangle| - |\langle \psi_{\text{L}} | H^\dagger | \psi_{\text{L}} \rangle|^2}{|\langle \psi_{\text{L}} | H H^\dagger | \psi_{\text{L}} \rangle|} \quad (\text{S39})$$

An exact right/left eigenvector $|\psi_{\text{R/L}}\rangle$ of H should have

$d_R(|\psi_R\rangle) = 0$ and $d_L(|\psi_L\rangle) = 0$. For $L = 8$, $h_z = J$, $d_R(|GS_R\rangle) = 1.4e-5$ and $d_L(|GS_L\rangle) = 1.0e-5$; and when $h_z = 2J$, $d_R(|GS_R\rangle) = 9.7e-5$ and $d_L(|GS_L\rangle) = 9.9e-5$. For $L = 24$, $d_R(|GS_R\rangle) = 3.0e-4$ and $d_L(|GS_L\rangle) = 4.0e-4$ for $h_z = J, \gamma = 0$, and $d_R(|GS_R\rangle) = 7.2e-4$ and $d_L(|GS_L\rangle) = 6.9e-4$ for $h_z = J, \gamma = 0.1J$. Thus we have verified the ground states used in our calculation are faithful ground states.

* songf18@mails.tsinghua.edu.cn

† jose.lado@aalto.fi

- [1] Although $A(E)$ is a complex-valued function, we can do Chebyshev expansion for its real and imaginary parts, respectively, then adding up the coefficients to get Eq. (S7).
- [2] A. Weiße, G. Wellein, A. Alvermann, and H. Fehske, The kernel polynomial method, *Rev. Mod. Phys.* **78**, 275 (2006).
- [3] H. G. Dawson, On the numerical value of $\int_0^h \exp(x^2) dx$, *Proceedings of the London Mathematical Society* **s1-29**, 519 (1897).
- [4] N. Hatano and D. R. Nelson, Localization transitions in non-hermitian quantum mechanics, *Phys. Rev. Lett.* **77**, 570 (1996).
- [5] N. Okuma and M. Sato, Hermitian zero modes protected by nonnormality: Application of pseudospectra, *Phys. Rev. B* **102**, 014203 (2020).
- [6] U. Schollwöck, The density-matrix renormalization group in the age of matrix product states, *Annals of Physics* **326**, 96 (2011), january 2011 Special Issue.
- [7] J. L. Lado and O. Zilberberg, Topological spin excitations in harper-heisenberg spin chains, *Phys. Rev. Research* **1**, 033009 (2019).
- [8] G. W. Stewart, A krylov–schur algorithm for large eigenproblems, *SIAM Journal on Matrix Analysis and Applications* **23**, 601 (2002).
- [9] T. Enss and U. Schollwöck, On the choice of the density matrix in the stochastic tmrg, *Journal of Physics A: Mathematical and General* **34**, 7769 (2001).
- [10] G. K.-L. Chan and T. Van Voorhis, Density-matrix renormalization-group algorithms with nonorthogonal orbitals and non-hermitian operators, and applications to polyenes, *The Journal of Chemical Physics* **122**, 204101 (2005).
- [11] D.-W. Zhang, Y.-L. Chen, G.-Q. Zhang, L.-J. Lang, Z. Li, and S.-L. Zhu, Skin superfluid, topological mott insulators, and asymmetric dynamics in an interacting non-hermitian aubry-andré-harper model, *Phys. Rev. B* **101**, 235150 (2020).
- [12] K. Yamamoto, M. Nakagawa, M. Tezuka, M. Ueda, and N. Kawakami, Universal properties of dissipative tomonaga-luttinger liquids: Case study of a non-hermitian xxz spin chain, *Phys. Rev. B* **105**, 205125 (2022).